



Design and commissioning of a wideband RF system for CSNS-II rapid-cycling synchrotron

Jian Wu^{1,2,3} · Xiang Li^{1,2,3} · Bin Wu^{2,3} · Chun-Lin Zhang^{2,3} · Yang Liu^{2,3} · Wei Long^{2,3} · Xiao Li^{1,2,3}

Received: 23 February 2023 / Revised: 20 July 2023 / Accepted: 6 August 2023 / Published online: 19 January 2024

© The Author(s), under exclusive licence to China Science Publishing & Media Ltd. (Science Press), Shanghai Institute of Applied Physics, the Chinese Academy of Sciences, Chinese Nuclear Society 2024

Abstract

The China Spallation Neutron Source (CSNS) upgrade project (CSNS-II) aims to enhance the beam power from 100 to 500 kW. A dual-harmonic accelerating method has been adopted to alleviate the stronger space-charge effect in rapid-cycling synchrotrons owing to the increased beam intensity. To satisfy the requirements of dual-harmonic acceleration, a new radio-frequency (RF) system based on a magnetic alloy-loaded cavity is proposed. This paper presents design considerations and experimental results regarding the performance evaluation of the proposed RF system through high-power tests and beam commissioning. The test results demonstrate that the RF system satisfies the desired specifications and affords significant benefits for CSNS-II.

Keywords Dual-harmonic acceleration · Magnetic alloy-loaded cavity · RF system

1 Introduction

The rapid-cycling synchrotron (RCS) in the China Spallation Neutron Source (CSNS) is dedicated to accelerating the proton beam from 80 MeV to 1.6 GeV [1, 2] and delivering a high-energy beam to the target station so as to generate neutrons for experiments and studies.

In the framework of the upgrade project (CSNS-II), the beam intensity will be increased from 1.56×10^{13} to 7.80×10^{13} protons per pulse (ppp) to achieve a higher beam power of 500 kW. However, a higher beam intensity results in a significant space-charge effect during the initial stages of acceleration; this poses a crucial challenge to both the transverse and longitudinal beam dynamics. To mitigate the space-charge effect, the injection energy of the RCS will be increased to 300 MeV. In addition, a dual-harmonic acceleration system [3, 4] will be adopted to achieve a uniform longitudinal beam distribution and large bunching factor, further alleviating the space-charge effect. Table 1 lists the main parameters of CSNS-II RCS. Although the CSNS-II project has not been officially initiated, R&D efforts and prototypes have been underway for a few years.

Figure 1 illustrates the voltage and frequency patterns of the fundamental and second harmonics during beam capture and acceleration according to the beam dynamics design. The fundamental harmonic has a peak voltage of 175 kV and operates over a period of 20 ms. In contrast, the second harmonic, with a peak voltage of 100 kV, is necessary only during the initial 6 ms of acceleration. This is because of the gradual weakening of the space-charge effect as the beam energy increases, rendering the maintenance of a high bunching factor with the second harmonic unnecessary [4]. The fundamental harmonic is provided by the ferrite-loaded

Jian Wu and Xiang Li contributed equally as co-first author.

This work was supported by funds from the National Natural Science Foundation of China (Nos. 11875270, U1832210, 12205317), Youth Innovation Promotion Association CAS (No. 2018015), and Guangdong Basic and Applied Basic Research Foundation (No. 2019B1515120046).

✉ Bin Wu
wubin@ihep.ac.cn

✉ Xiao Li
lixiao@ihep.ac.cn

¹ University of Chinese Academy of Sciences, Beijing 100049, China

² Institute of High Energy Physics, Chinese Academy of Sciences, Beijing 100049, China

³ Spallation Neutron Source Science Center, Dongguan 523803, China

Table 1 Main parameters of the CSNS-II RCS

Parameters	Values
Ring circumference (m)	227.92
Injection energy (MeV)	300
Extraction energy (GeV)	1.6
Beam power (kW)	500
RF cavities	8 ($H=2$) + 3 ($H=4$)
RF voltages	175 kV ($H=2$) + 100 kV ($H=4$)
Number of bunches	2
Repetition rate (Hz)	25
Repetition period (ms)	20
Number of protons (ppp)	7.80×10^{13}

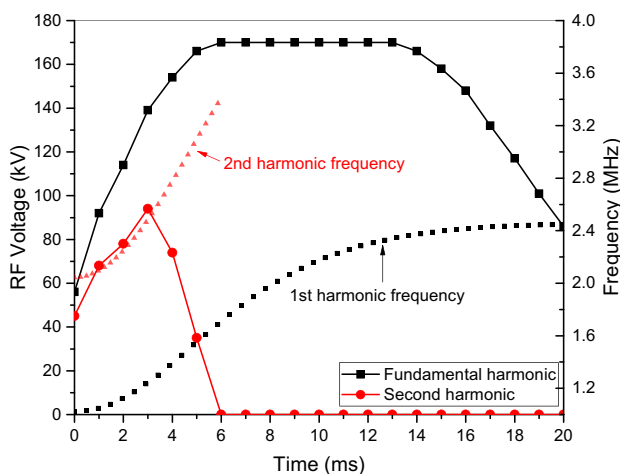


Fig. 1 RF voltages and frequency of the dual-harmonic RF system in 20 ms. The left vertical axis represents the total RF voltage, while the right vertical axis corresponds to the operating frequency of the RF cavity

cavity; whereas, the second harmonic should be achieved by a higher-gradient radiofrequency (RF) cavity. This is because the reserved space in the ring is not sufficient for adopting ferrite-loaded cavities because of its low saturation flux density.

The magnetic alloy (MA) core-loaded cavity has emerged as a promising solution for achieving high-gradient acceleration, as demonstrated in facilities such as J-PARC [5, 6], HIAF [7] and XiPAF [8], where the operation and test results have showcased its effectiveness. This is attributed to the remarkable saturation flux density and permeability of the MA cores [9, 10]. In addition, the MA cores possess a low Q value, which contributes to their wideband characteristics. This facilitates the realization of a simpler tuning-free RF system and enables the generation of multiple harmonics. Therefore, the MA-loaded cavity was selected for

CSNS-II [11]. A prototype of the cavity has been developed and tested using a beam.

However, the wideband property of the MA-loaded cavity, along with the RF power source operating in class AB1 and the effect of beam loading, results in the generation of multiple harmonics in the cavity voltage [12]. Compensation for higher harmonics is crucial to ensure stable beam acceleration [13, 14]. This poses a challenge in achieving a high-gradient operation of the cavity while effectively suppressing the high harmonics. Therefore, careful consideration of the RF system design is required.

In this paper, we present a new RF system for a CSNS-II RCS that utilizes an MA-loaded cavity. We herein provide detailed information on the configuration of the RF system and describe an evaluation of its performance through comprehensive high-power tests during the formal operation of the CSNS-II RCS. The experimental results afford valuable insights for future system optimization. Furthermore, we detail beam commissioning experiments performed with the proposed RF system providing both the fundamental and second harmonic RF voltages. The results of beam commissioning are also presented.

2 Design of the RF system

2.1 High-gradient MA-loaded cavity

Similar to the ferrite-loaded cavity [15], the MA-loaded cavity consists of three $\lambda/4$ double resonators with three accelerating gaps that are connected in series from the viewpoint of the beam. Meanwhile, the double resonators are coupled in parallel with low impedance to the RF power source. Figure 2 shows a schematic of an MA-loaded cavity. Each $\lambda/4$ resonator is a water tank loaded with three MA cores. The tanks on the same side of the gaps are connected in parallel via copper bars. Sampling capacitors are strategically placed on both sides of the gaps to measure the RF voltage. These data are then transmitted to a low-level RF (LLRF) system for feedback control and monitoring. The essential cavity parameters are listed in Table 2.

The design of compact gap structures having high withstanding voltages is crucial for achieving high acceleration gradients. Figure 3 presents the profile of the newly designed gap structure, which is identical to the other two gaps in the MA-loaded cavity. The gap is a toroid fabricated from 95% alumina micropowder by using a high-temperature sintering process. It has an outer diameter of 108 mm ($R1$), an inner diameter of 96 mm ($R2$), and a length of 70 mm. Two stainless steel pipes are inserted into the ceramic with 40-mm spacing between them.

This design effectively reduces the electric field on the ceramic surface along the air side and ensures a short transit

Fig. 2 (Color online) Structure diagram of the MA-loaded cavity

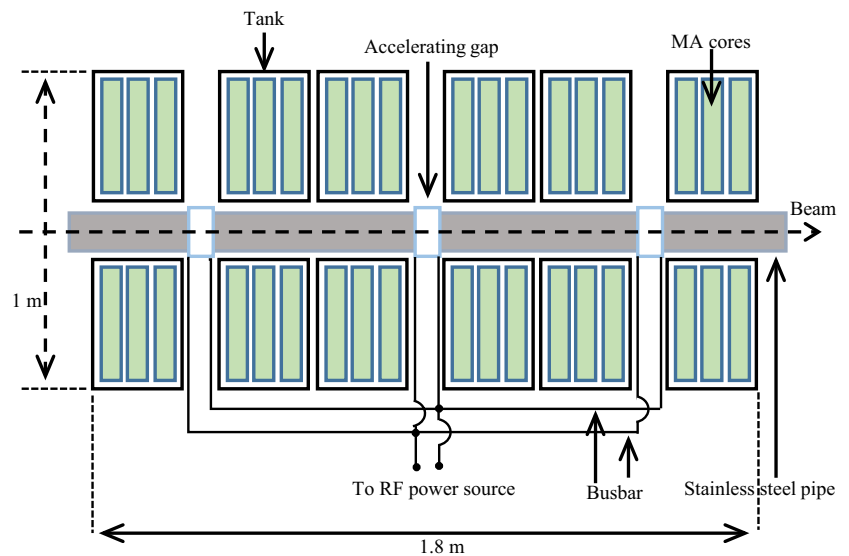


Table 2 Main parameters of the MA-loaded cavity

Parameters	Values
Cavity length (m)	1.8
Peak acceleration gradient (kV/m)	40
Fundamental harmonic frequency (MHz)	1.02–2.44
Second harmonic frequency (MHz)	2.04–3.4 (0–6 ms)
Number of gaps per cavity	3
Number of tanks	6
Number of MA cores per tank	3
Core outer diameter (mm)	850
Core inner diameter (mm)	316
Core thickness (mm)	25
Power dissipation per cavity (kW)	72
Type of MA core cooling	Water cooling
Maximum/Minimum impedance (Ω)	250 /100

time for the beam in a vacuum. The withstanding voltage property of this gap structure was validated using a high-voltage test, as discussed in Sect. 3. The stainless steel pipes are securely welded to a ceramic toroid using Kovar. Two copper rings near the gap are soldered onto the surface of the stainless steel pipes, providing a connection between the copper bars and the RF power source. This arrangement generates a large RF electric field between the stainless steel pipes for beam acceleration, as depicted in Fig. 3.

2.2 RF power source

To achieve the high gradient required for this compact cavity design, a two-stage amplifier configuration is employed, as shown in Fig. 4. The final amplifier consists of two high-power tetrode tubes operating in the push–pull mode,

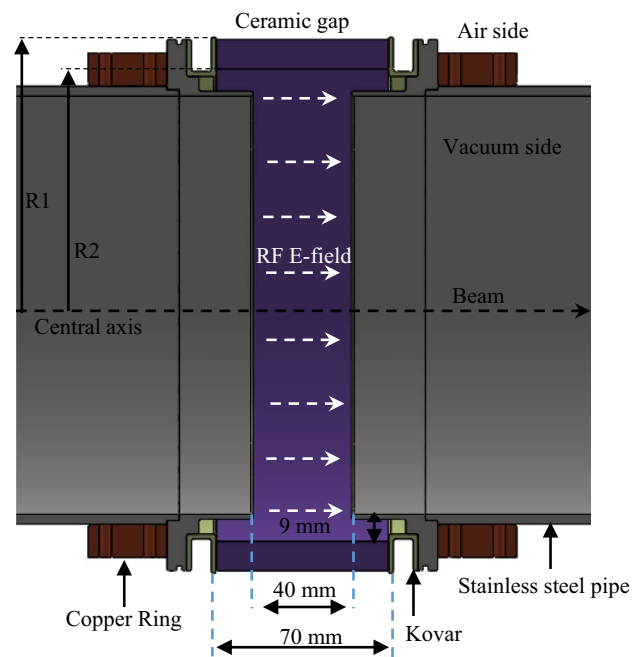


Fig. 3 (Color online) Cut view of an accelerating gap structure

directly connected to the copper rings on each side of the ceramic gaps, as shown in Fig. 2. Because the MA-loaded cavity operates in multiharmonic mode, a solid-state amplifier (SSA) with a bandwidth of 1–8 MHz is utilized as the driver stage. An impedance-matching network is implemented to ensure effective signal transmission between the SSA and tetrode tubes. The LC filter circuits are parallel to the grid, screen, and anode of the tetrode tubes to prevent the RF components from flowing backward into the power supply. DC cut capacitors of approximately 20 nF are installed

Fig. 4 Block diagram of the RF power system

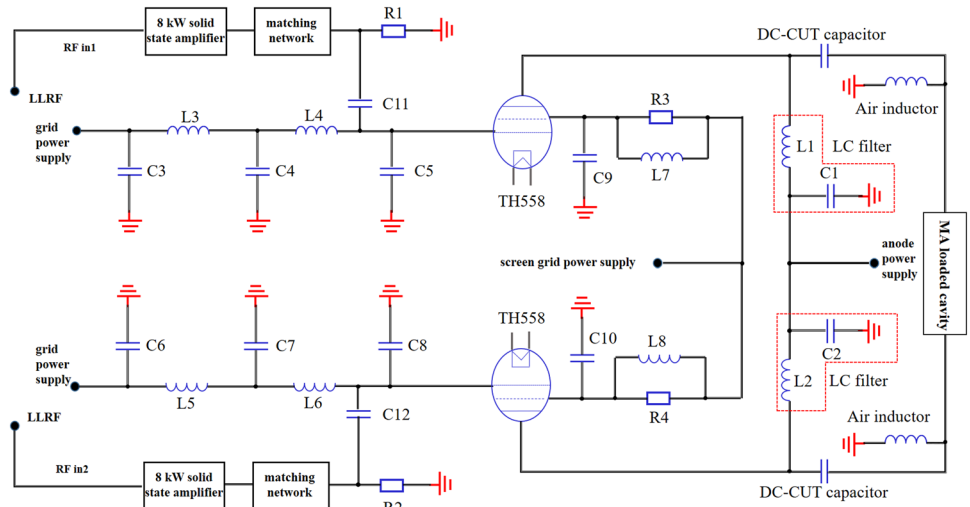


Table 3 Main parameters of the RF power system

Parameters	Values
Frequency range (MHz)	1–8
Final stage amplifier	Tetrode tube (TH558)
Repetition frequency (Hz)	25
Duty cycle	50%
Anode dissipation (kW)	500
Screen grid dissipation (kW)	8
Control grid dissipation (kW)	3
DC anode voltage (kV)	15
DC screen grid voltage (V)	1500
DC control grid voltage (V)	–340

between the cavity and the tetrode tubes, allowing only the RF current to be fed into the cavity. The detailed parameters of the RF system are listed in Table 3.

The two tetrode tubes are operated in class AB1 to ensure an appropriate work efficiency. However, owing to the cut-off of the anode current and wideband impedance of the cavity, the voltage in the MA-loaded cavity contains rich higher harmonics [16]. These higher harmonics introduce additional power dissipation into the cavity and impose limitations on the cavity gradient, which must be effectively suppressed by the LLRF control system.

Nevertheless, the working efficiency of the tetrode tube is constrained by the relatively low impedance of the cavity within the operating frequency range of the RF system, as indicated by the solid black line in Fig. 5. The horizontal axis represents the tested frequency and the vertical axis represents the absolute value of the load impedance of the tetrode tube. The shaded area corresponds to the operating frequency range of the RF system. To address this limitation,

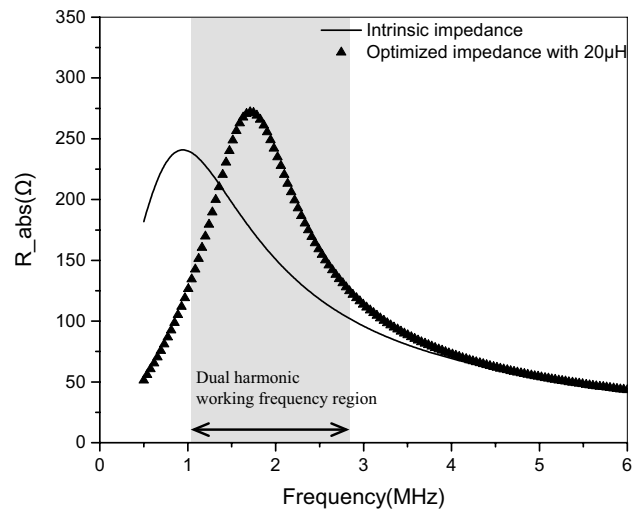


Fig. 5 Load impedance of the tetrode tube before and after optimization

an inductor is connected in parallel to the cavity to enhance its impedance, as detailed in a prior work [17]. Two air inductors with an optimized value of 20 μH are designed, manufactured, and installed in the final stage cabinet, parallel to the DC cut capacitors, as illustrated in Fig. 4. The load impedance of the tetrode tube after optimization is indicated by the scattered triangles in Fig. 5. Evidently, the load impedance significantly increases within the working frequency range. The improvement in the tetrode tube efficiency was demonstrated through high-power tests.

2.3 LLRF control system

As aforementioned, the suppression of higher harmonics in the MA-loaded cavity is crucial. To ensure stable operation of the entire RF system and effective harmonic suppression,

a multiharmonic feedback control algorithm was developed. Unlike the control logic employed in the J-PARC RCS [18], our approach enables the independent control of the two tetrode tubes, with the LLRF system managing the two separate RF drive signals. The LLRF control system for the MA-loaded cavity is simpler compared to the control system used for the ferrite-loaded cavity in the CSNS RCS [19], as it does not require an active tuning loop. A block diagram of the LLRF system is presented in Fig. 6.

As shown in Fig. 6, the pickup signal is directly sampled by an analog-to-digital converter (ADC) and forwarded to the feedback block for each harmonic, with the regulation extending up to $H=12$. The feedback module adopts a classic in-phase/quadrature-phase (I/Q) feedback structure. The I/Q set values are transformed using the programmed data of the amplitude and phase of the RF signal. A direct digital synthesizer (DDS) is used in both the demodulation and modulation modules to generate sine and cosine signals with unity amplitude owing to its high accuracy. The I/Q components are filtered using digital filters and compared with their set values to calculate the I/Q errors. These errors are regulated using a proportional–integral (PI) feedback (FB) controller. Additionally, to enhance the tracking performance, the feedforward module generates feedforward components using an adaptive feedforward algorithm (implemented exclusively for driving harmonics). The combined feedforward and feedback output signals are amplified and transmitted to the RF cavity. The phase offset signal compensates for the phase response of the I/Q feedback loop, which is crucial for maintaining a stable feedback control. All the modules are implemented in a field-programmable gate array (FPGA) using digital circuits operating at a frequency of 60 MHz. With the support of adequate FPGA memory, the I/Q waveform of each harmonic is recorded not only for commissioning and monitoring the feedback but also for further analysis.

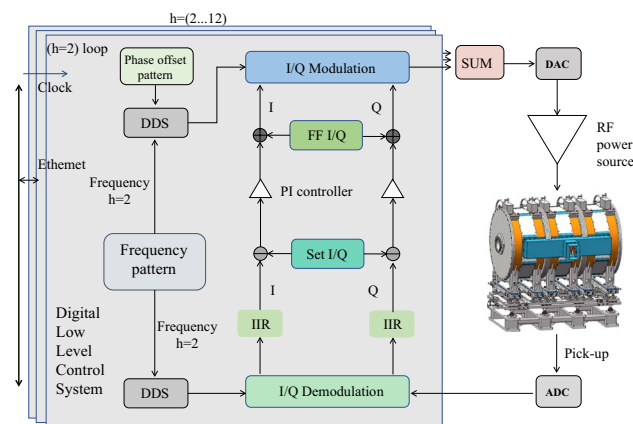


Fig. 6 (Color online) Block diagram of the LLRF system

The requirement for the multiharmonic feedback control is to maintain higher harmonics below 1 kV, while for the fundamental voltage, the amplitude ripple and phase ripple should be controlled to $\pm 1.0\%$ and $\pm 1^\circ$, respectively.

3 High-power test results

Because the MA-loaded cavity exhibits the potential to function as a fundamental cavity by appropriately selecting the Q value, the dynamic response characteristics of the RF system under both fundamental and second harmonic sweeping modes for the CSNS-II RCS were examined through high-power experiments. These experiments encompassed various aspects, including a maximum acceleration gradient test of the MA-loaded cavity, evaluation of the harmonic compensation performance, and assessment of the control accuracy pertaining to the amplitude and phase of the LLRF control system.

3.1 RF test system configuration

The RF system test stand and its key components are depicted in Fig. 7, which provides a comprehensive overview of the experimental setup. Figure 7a shows the MA-loaded cavity, marking thermometers, and flowmeters at each tank outlet to facilitate temperature rise monitoring. As shown in Fig. 7b, the final stage cabinet houses two tetrode tubes, with each tube connected in series with a DC-cut capacitor and in parallel with an LC filter circuit. Air conductors, which are essential for optimizing the load impedance of the tetrode tube, are parallel to the DC-cut capacitor. The SSAs and LLRF control systems are illustrated in Fig. 7c and d, respectively. Figure 7e shows the power supply responsible for energizing the entire RF system.

To ensure the successful execution of the high-power tests, specific operating parameters were defined for the RF power source, as outlined in Table 3. These parameters serve as critical guidelines for maintaining a stable and reliable operation during the experimental phase.

3.2 Maximum field gradient tests

The highest acceleration gradient in the MA-loaded cavity was observed in the second harmonic sweeping mode. Figure 8 presents the voltage waveforms captured at the ends of the acceleration gap, referred to as ‘upstream’ and ‘downstream’. Notably, the RF voltage waveforms at both ends exhibited the same amplitude but opposite phases because of the push–pull operation mode. The synthetic voltage reflects the voltage difference between the two gap ends and corresponds to the acceleration voltage experienced by the beam during its traversal through the gap.

Fig. 7 (Color online) High-power test stand and details show. **a** MA-loaded cavity. **b** Tetrode tubes in the final stage cabinet. **c** LLRF control system. **d** SSAs. **e** RF power supplier system

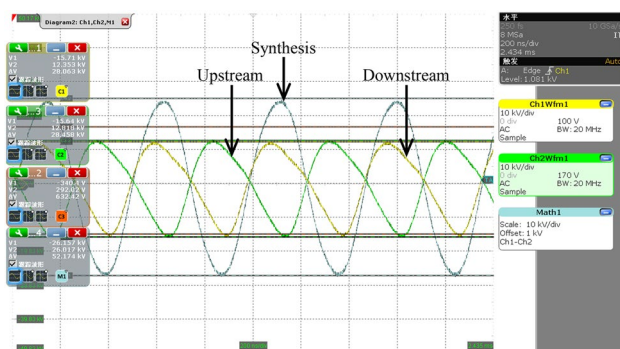
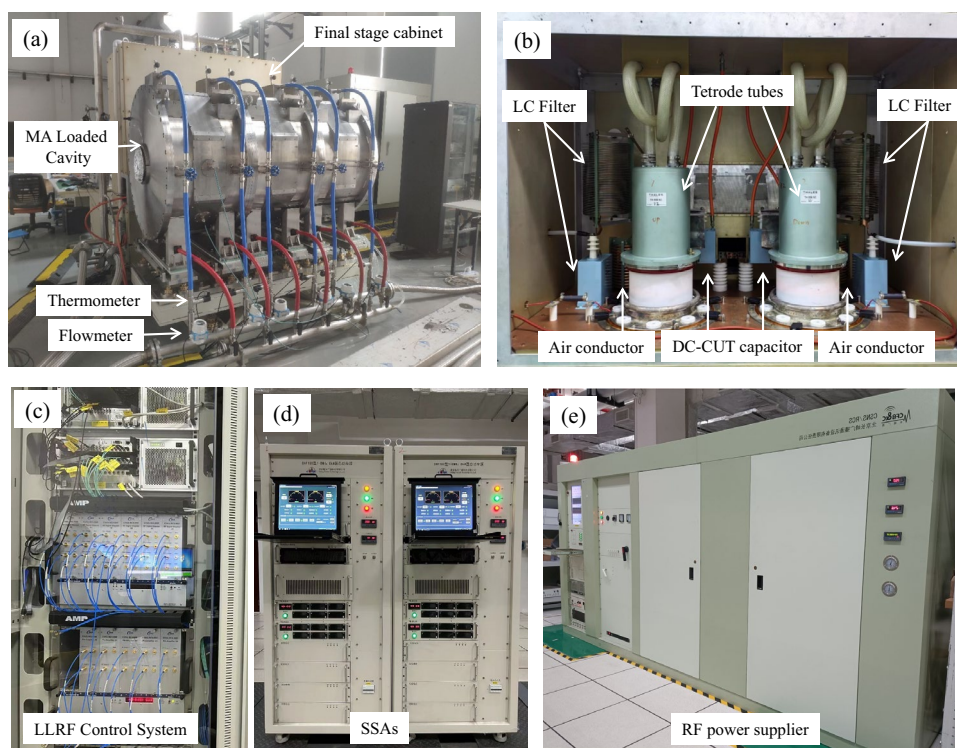


Fig. 8 (Color online) Voltage waveforms in the both sides of an accelerating gap. The synthesized waveform is obtained through the subtraction of these two waveforms

Remarkably, we achieved a peak synthetic voltage of 72 kV (26 kV per gap) without gap flashover. This noteworthy result translates to an impressive acceleration gradient of approximately 43 kV/m, surpassing the gradient achieved by the ferrite-loaded cavity, making it highly suitable for applications within the CSNS-II RCS. However, further gradient enhancement of the MA-loaded cavity was not achieved owing to the occurrence of screen-grid overcurrent in the tetrode tube. To address this issue, we devised plans to upgrade the anode power supply of the tetrode tube, thus paving the way for future improvements.

However, in fundamental harmonic sweeping mode, the acceleration gradient is lowered by the power dissipation of

the cavity, primarily resulting from a high duty cycle reaching up to 50%. The power dissipation of the cavity is calculated using the temperature increase and flow rate [20]. The maximum peak voltage supplied by the cavity is only approximately 39.5 kV, corresponding to an acceleration gradient of approximately 22 kV/m. The cavity power dissipation reaches approximately 72 kW, which is close to the safety threshold for the cooling capacity of the cavity [21].

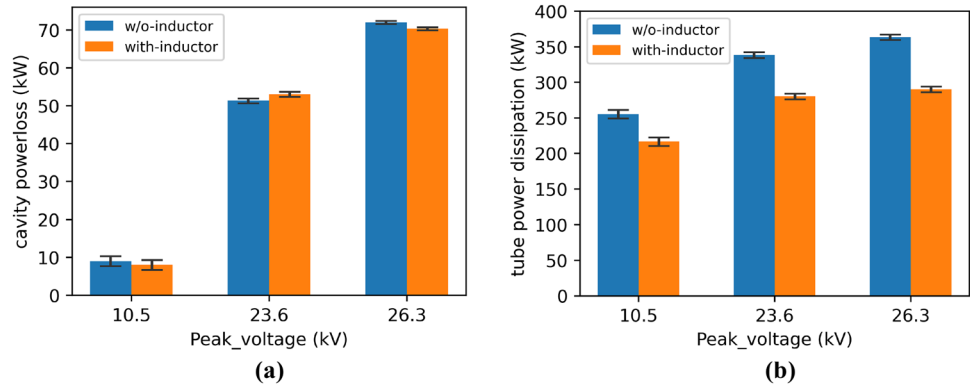
3.3 Inductor impacts tests

Furthermore, we investigated the impact of the designed inductor on power dissipation reduction for both the cavity and tetrode tubes. Figure 9a and b indicate that the installed inductor has a minimal effect on the cavity power dissipation; whereas, it significantly reduces the power consumption of the tetrode tubes. This observation can be attributed to the optimized load impedance of the tetrode tubes within the operating band, as shown in Fig. 5, which decreases the output current. Conversely, the power dissipation of the cavity remained relatively unaffected, as it is primarily determined by the cavity voltage (V) and the shunt impedance (R_p) of the cavity [9].

$$P = V^2/2R_p \quad (1)$$

Here, R_p primarily depends on the performance of the MA core. Because V is controlled by the LLRF control

Fig. 9 (Color online) High-power test results of the RF system under the fundamental sweeping mode. **a** Power dissipation of the MA-loaded cavity with and without the air conductor installation of different peak voltage. **b** Power dissipation of the tetrode tubes with and without the air conductor installation of different peak voltage



system, extremely small changes in its harmonic components occur after the installation of the air inductor. By delivering the required cavity voltage while reducing the output current, the tetrode tube exhibits improved load-driving capability. This experiment highlights the significance of optimizing the load impedance as it enhances the performance and efficiency of the RF system.

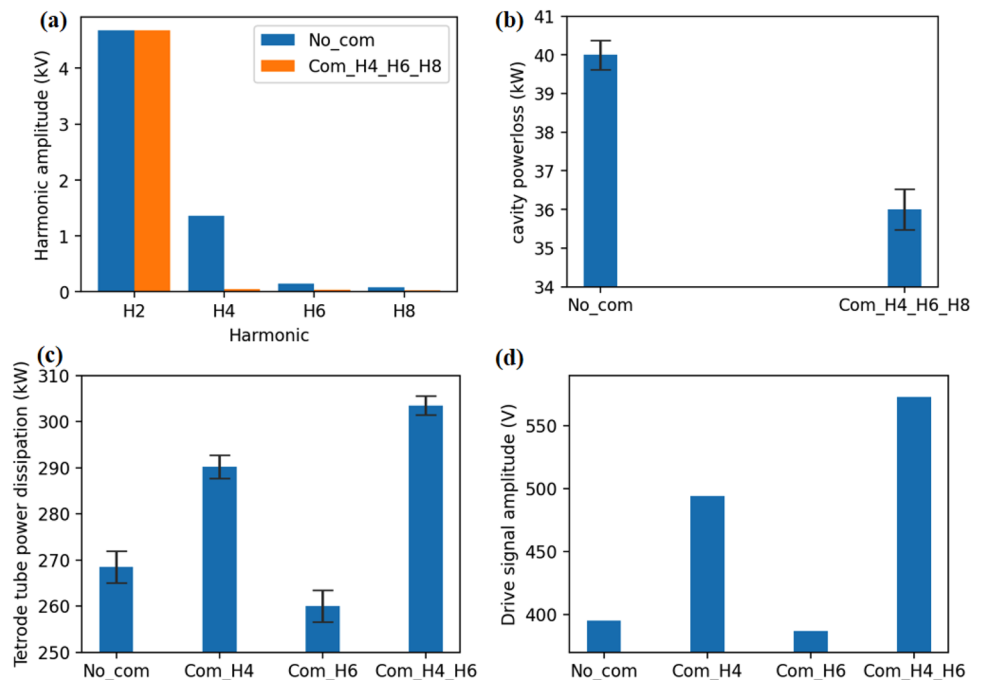
3.4 Higher harmonics suppression tests

Although the synthesized voltage waveform appears as a nearly pure sinusoidal wave in Fig. 8, the RF voltage waveform selected at both the upstream and downstream ends of the cavity contains several harmonics. The presence of higher harmonics does not contribute to beam acceleration but increases cavity power dissipation. Therefore,

compensating for these harmonics by using an LLRF control system is necessary.

For brevity, only the test results for the fundamental sweeping mode are presented herein. In this mode, the peak voltage tested was set at 28 kV, corresponding to an upstream and downstream voltage amplitude of 4.7 kV in each gap, as indicated by the fundamental component ($H=2$) in Fig. 10a. The horizontal axis represents the harmonic number; whereas, the vertical axis shows the amplitude of each harmonic calculated using the fast Fourier transform (FFT) analysis. Evidently, the second harmonic ($H=4$) was prominent prior to applying feedback control. However, the amplitudes of the higher harmonics ($H=4, 6,$ and 8) were effectively suppressed after applying the feedback control, as indicated by the orange bars in Fig. 10a. Moreover, Fig. 10b shows that the cavity power dissipation decreased by approximately 10%. This decrease in power

Fig. 10 (Color online) Higher harmonics suppression test results of the RF system under the fundamental sweeping mode. **a** Harmonic components of the test voltage before and after harmonics compensation. **b** Cavity power dissipation before and after harmonic compensation. **c** and **d** Power dissipation of the tetrode tubes and the driven signal amplitude to the tetrode tubes with different order of harmonic compensation



dissipation can facilitate further improvement of the cavity gradient during high-duty-cycle operation, which will be verified in the future via an upgrade of the RF power source supply system.

In addition, interestingly, the state of the tetrode tube was observed to be associated with the order of harmonic compensation, as depicted in Fig. 10c, d. The horizontal axis represents the order of the harmonic compensation; whereas, the vertical axis denotes the power dissipation of the tetrode tubes and the signal amplitude driven to the tetrode tubes. The results indicate that compensating for the even harmonic ($H=4$) leads to a significant increase in tetrode tube power dissipation and driven signal amplitude. This phenomenon will be further investigated through high-power tests and numerical analysis of the tetrode tube operation in the future.

3.5 Amplitude and phase stability tests

In addition to higher harmonic compensation, ensuring the stability of the programmed RF voltage during the fundamental and second harmonic sweeping modes is crucial for stable beam acceleration in the CSNS-II RCS. The voltage amplitude envelope of each cycle under these two modes is shown in Fig. 1, with peak voltages of 28 and 72 kV. When only feedback control is applied, the amplitude and phase are poorly controlled in either mode, as indicated by the red lines in Fig. 11a–d. For the fundamental mode, the peak-to-peak stability of the amplitude is worse than -2% to $+2\%$, and that of the phase is worse than -0.5° to 2° ; the requirements are therefore not satisfied. The stability appears to be worse in the second harmonic mode. Although increasing the feedback gain is a common approach to improve

peak-to-peak stability, it may increase the risk of instability and degrade the noise level. Thus, alternative control algorithms need to be developed to enhance the tracking performance. In this regard, adaptive feedforward control is a promising candidate because the RF voltage is repeated in every cycle. The feedforward component of each cycle is the sum of the feedback and feedforward components of the previous cycle. The long-term stability of adaptive feedforward control has been validated in an RF system based on a ferrite-loaded cavity [15].

With the combined effect of the feedback and feedforward control, the amplitude and phase dynamic control errors in one cycle are improved to within $\pm 1\%$ and $\pm 1^\circ$ for both modes, as indicated by the green lines in Fig. 11a–d, satisfying the RF system design requirement.

4 Beam commissioning results

The performance of the new RF system based on the MA-loaded cavity was further validated during actual beam operation by meticulously selecting the working point of the tetrode tube. With the invaluable assistance of the CSNS beam commissioning group, the new RF system was successfully and officially operated. During the beam commissioning process, the ferrite-loaded cavity supplied the fundamental voltage for beam acceleration, as shown in Fig. 1. However, the disparity between the second harmonic voltage provided by the MA-loaded cavity, as depicted in Fig. 12, and that shown in Fig. 1 must be noted. This discrepancy arises because of the utilization of a single MA-loaded cavity in this particular case, resulting in a different voltage

Fig. 11 **a** Amplitude dynamic control errors of fundamental in one cycle. **b** Phase dynamic control errors of fundamental in one cycle. **c** Amplitude dynamic control errors of second harmonic in one cycle. **d** Phase dynamic control errors of second harmonic in one cycle. Here, ‘FB’ denotes feedback control; while, ‘FF’ denotes feedforward control

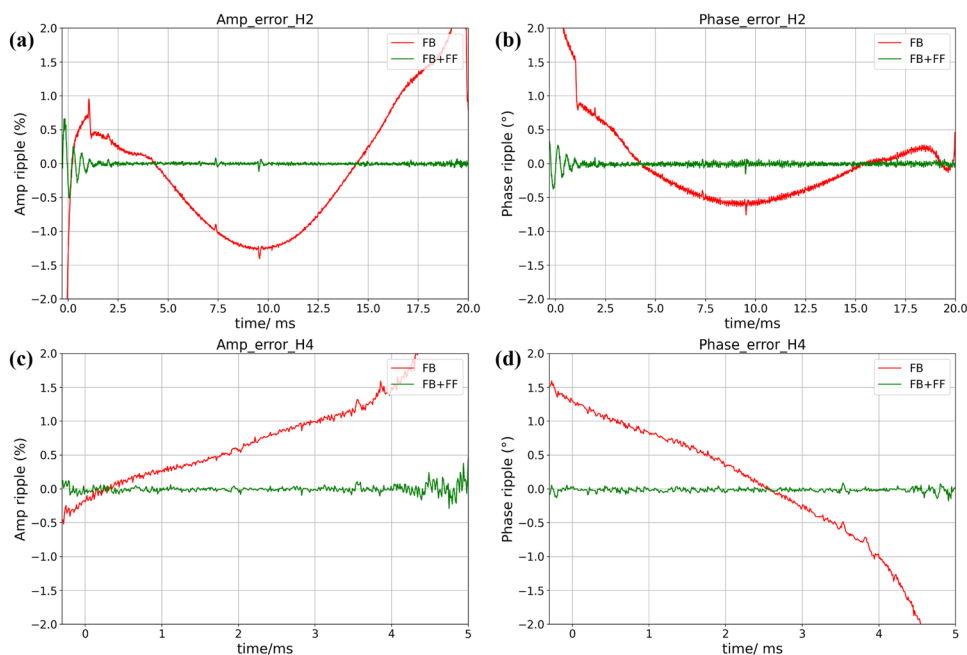
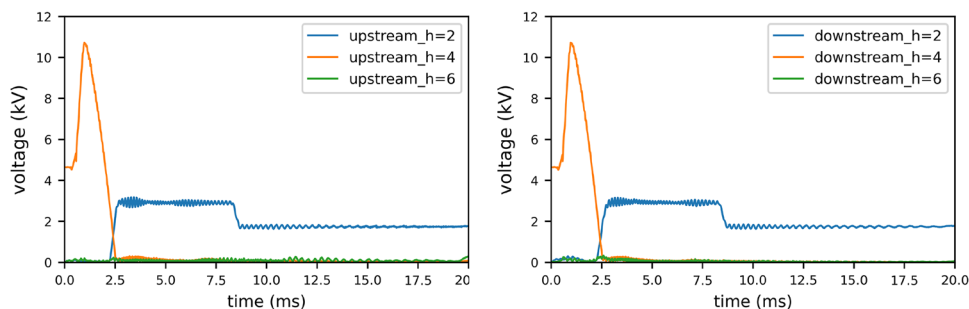


Fig. 12 Voltage captured at the upstream end (left) and downstream end (right) of one gap of the cavity



pattern than when three MA-loaded cavities were employed. The second-harmonic generation was activated only during the initial 2.5 ms of acceleration, with a maximum voltage of approximately 22 kV/gap (11 kV for each end). To reduce the beam loss in the arc region and mitigate the beam instability, it was necessary to increase the fundamental voltage after 2 ms to lower the bunching factor. Consequently, the MA-loaded cavity supplied a maximum fundamental voltage of approximately 6 kV/gap.

The beam loading was compensated for up to the third harmonic ($H=6$); it is evident from Fig. 12 that the third harmonics, both upstream and downstream, were effectively suppressed below 0.7 kV/gap, indicating the effectiveness of the multiharmonic feedback control. However, small oscillations notably appeared on the fundamental voltage, as shown in Fig. 12. Adaptive feedforward control was not applied during the beam commissioning phase; its implementation may help suppress these oscillations in the future.

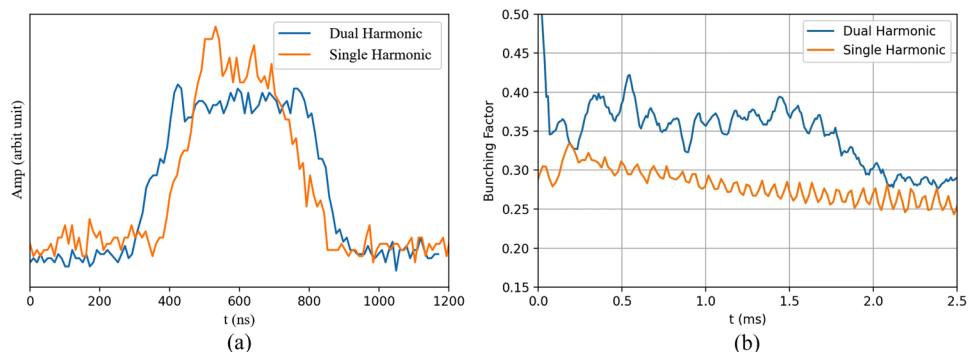
With the operation of the dual-harmonic acceleration system, the longitudinal distribution of bunches became more uniform. The bunch shape is shown in Fig. 13a. In this scenario, the bunch factor, as shown in Fig. 13b, exhibited a significant increase during the initial stages of acceleration as compared to the case of single harmonic acceleration. This enhancement in the bunching factor effectively reduced the space-charge effect, allowing for an increase in the beam intensity from 1.95×10^{13} to 2.184×10^{13} ppp for the two bunches. Consequently, the beam power has been successfully increased to 140 kW since the commencement

of daily operation of the dual-harmonic acceleration system in March 2023. These results underscore the significant progress achieved through the development of the RF system based on the MA-loaded cavity for CSNS-II.

5 Summary

A prototype MA-loaded cavity was developed for dual-harmonic acceleration in the CSNS-II RCS. An impressive maximum acceleration gradient of 43 kV/m was achieved. Through the successful commissioning of the multiharmonic feedback control, the distortion in the voltage waveform resulting from the wideband nature of the cavity and the dynamic characteristics of the tetrode tube was effectively mitigated. This ensures the stability and reliability of the RF systems. The performance of the RF system during the beam commissioning phase was extensively validated. The utilization of the dual-harmonic acceleration led to a significant increase in the bunching factor and beam power. This noteworthy achievement has contributed to the advancement of CSNS, laying the foundation for its further development.

Fig. 13 **a** Comparison of the beam longitudinal distributions between the dual-harmonic and single harmonic modes. **b** Comparison of the bunching factor between the dual-harmonic and single harmonic modes from 0 to 2.5 ms



Acknowledgements The authors express their gratitude to the CSNS beam commissioning group for their invaluable assistance and comments.

Author contributions All authors contributed to the study conception and design. Material preparation, data collection and analysis were performed by JW, XL and BW. The first draft of the manuscript was written by JW and all authors commented on previous versions of the manuscript. All authors read and approved the final manuscript.

Data availability The data that support the findings of this study are openly available in Science Data Bank at <https://cstr.cn/31253.11.sciencedb.14213> and <https://www.doi.org/10.57760/sciencedb.14213>.

Declarations

Conflict of interest The authors declare that they have no competing interests.

References

1. S. Wang, S.X. Fang, S.N. Fu et al., Introduction to the overall physics design of CSNS accelerators. *Chinese Phys. C* **33**, 1 (2009). <https://doi.org/10.1088/1674-1137/33/S2/001>
2. S. Wang, Y.W. An, S.X. Fang et al., An overview of design for CSNS/RCS and beam transport. *Sci. China Phys. Mech.* **54**, 239–244 (2011). <https://doi.org/10.1007/s11433-011-4564-x>
3. J.F. Chen, J.Y. Tang, Studies of dual-harmonic acceleration at CSNS. *Chinese Phys C* **34**, 1643 (2010). <https://doi.org/10.1088/1674-1137/34/10/018>
4. H.Y. Liu, S. Wang, Longitudinal beam dynamic design of 500 kW beam power upgrade for CSNS-II RCS. *Radiat. Detect. Technol. Methods* **6**, 339–348 (2022). <https://doi.org/10.1007/s41605-022-00325-5>
5. M. Yamamoto, K. Hasegawa, M. Yoshii et al., High power test of MA cavity for J-PARC RCS. In: 2007 IEEE particle accelerator conference (PAC). 1532–1534 (2007). <https://doi.org/10.1109/PAC.2007.4440813>
6. C. Ohmori, E. Ezura, K. Hara et al., Development of a high gradient rf system using a nanocrystalline soft magnetic alloy. *Phys. Rev. Spec. Top-Ac.* **16**, 112002 (2013). <https://doi.org/10.1103/PhysRevSTAB.16.112002>
7. K. Wang, Z. Xu, P. Jin P, et al., Design of the deceleration magnetic alloy cavity for a high-intensity heavy-ion accelerator facility spectrometer Ring. *Nucl. Instrum. Meth. A.* **1005**, 165364 (2021). <https://doi.org/10.1016/j.nima.2021.165364>
8. G.R. Li, S.X. Zheng, H.J. Zeng et al., Design and test of an RF acceleration system loaded with magnetic alloy for the proton synchrotron of the Xi'an proton application facility. *Nucl. Sci. Tech.* **29**, 94 (2018). <https://doi.org/10.1007/s41365-018-0434-9>
9. B. Wu, X. Li, Z. Li et al., Development of a large nanocrystalline soft magnetic alloy core with high μ_Q products for CSNS-II. *Nucl. Sci. Tech.* **33**, 99 (2022). <https://doi.org/10.1007/s41365-022-01087-x>
10. K. Suzuki, A. Makino, A. Inoue et al., Soft magnetic properties of nanocrystalline bcc Fe–Zr–B and Fe–M–B–Cu (M=transition metal) alloys with high saturation magnetization (invited). *J. Appl. Phys.* **70**, 6232–6237 (1991). <https://doi.org/10.1063/1.350006>
11. B. Wu, X. Li, C.L. Zhang et al., Design and verification of a high-gradient and high-power 2nd harmonic cavity for the China spallation neutron source upgrade project. *Rev. Sci. Instrum.* **94**, 043301 (2023). <https://doi.org/10.1063/5.0141079>
12. B. Wu, H. Sun, X. Li et al., Higher harmonic voltage analysis of magnetic-alloy cavity for CSNS/RCS upgrade project. *Radiat. Detect. Technol Methods* **4**, 293–302 (2022). <https://doi.org/10.1007/s41605-020-00183-z>
13. F. Tamura, M. Yamamoto, C. Ohmori et al., Multiharmonic rf feedforward system for beam loading compensation in wide-band cavities of a rapid cycling synchrotron. *Phys. Rev. Spec. Top-Ac.* **14**, 051004 (2011). <https://doi.org/10.1103/PhysRevSTAB.14.051004>
14. F. Tamura, M. Yamamoto, Y. Sugiyama et al., Simulations of beam loading compensation in a wideband accelerating cavity using a circuit simulator including a LLRF feedback control. *J. Phys. Conf. Ser.* **1350**, 012189 (2019). <https://doi.org/10.1088/1742-6596/1350/1/012189>
15. X. Li, H. Sun, C.L. Zhang et al., Design of rapid tuning system for a ferrite-loaded cavity. *Radiat. Detect. Technol Methods* **5**, 324–331 (2021). <https://doi.org/10.1007/s41605-021-00255-8>
16. B. Wu, J. Wu, X. Li et al., Operation analysis of high power tetrode tube for the wideband cavity in CSNS-II. *IEEE T. Nucl. Sci.* **70**, 2388–2396 (2023). <https://doi.org/10.1109/TNS.2023.3321613>
17. A. Schnase, K. Hasegawa, M. Nomura et al., MA Cavities for J-PARC with controlled Q-value by external inductor. 2007 IEEE particle accelerator conference (PAC). 2131–2133 (2007). <https://doi.org/10.1109/pac.2007.4441173>
18. F. Tamura, Y. Sugiyama, M. Yoshii et al., Development of next-generation LLRF control system for J-PARC rapid cycling synchrotron. *IEEE T. Nucl. Sci.* **66**, 1242–1248 (2019). <https://doi.org/10.1109/TNS.2019.2899358>
19. X. Li, H. Sun, W. Long et al., Design and performance of the LLRF system for CSNS/RCS. *Chinese Phys. C* **39**, 027002 (2015). <https://doi.org/10.1088/1674-1137/39/2/027002>
20. M. Yuichi, T. Kageyama, Development of medium-frequency cavity loaded with multi-ring magnetic alloy cores cooled by chemically inert liquid. *Nucl. Instrum. Meth. A* **1010**, 165525 (2021). <https://doi.org/10.1016/j.nima.2021.165525>
21. T. Uesugi, Y. Mori, C. Ohmori et al., Direct-cooling MA cavity for J-PARC synchrotrons. Proceedings of the 2003 particle accelerator conference. 1234–1236 (2003). <https://doi.org/10.1109/PAC.2003.1289663>

Springer Nature or its licensor (e.g. a society or other partner) holds exclusive rights to this article under a publishing agreement with the author(s) or other rightsholder(s); author self-archiving of the accepted manuscript version of this article is solely governed by the terms of such publishing agreement and applicable law.